Journal of Computational Physics 399 (2019) 108952

Contents lists available at ScienceDirect

Journal of Computational Physics

www.elsevier.com/locate/jcp

Semi-implicit methods for the dynamics of elastic sheets

Silas Alben [a,*], Alex A. Gorodetsky [b], Donghak Kim [b], Robert D. Deegan [c]

[a] Department of Mathematics, University of Michigan, Ann Arbor, MI 48109, USA
[b] Department of Aerospace Engineering, University of Michigan, Ann Arbor, MI 48109, USA
[c] Department of Physics & Center for the Study of Complex Systems, University of Michigan, Ann Arbor, MI 48109, USA

ARTICLE INFO

Article history:
Received 18 April 2019
Received in revised form 6 September 2019
Accepted 9 September 2019
Available online 16 September 2019

Keywords:
Elastic
Buckling
Dynamics
Semi-implicit
Bending
Stretching

ABSTRACT

Recent applications (e.g. active gels and self-assembly of elastic sheets) motivate the need to efficiently simulate the dynamics of thin elastic sheets. We present semi-implicit time stepping algorithms to improve the time step constraints that arise in explicit methods while avoiding much of the complexity of fully-implicit approaches. For a triangular lattice discretization with stretching and bending springs, our semi-implicit approach involves discrete Laplacian and biharmonic operators, and is stable for all time steps in the case of overdamped dynamics. For a more general finite-difference formulation that can allow for general elastic constants, we use the analogous approach on a square grid, and find that the largest stable time step is two to three orders of magnitude greater than for an explicit scheme. For a model problem with a radial traveling wave form of the reference metric, we find transitions from quasi-periodic to chaotic dynamics as the sheet thickness is reduced, wave amplitude is increased, and damping constant is reduced.

1. Introduction

In recent years there have been various studies of how spatial variations in the composition of a thin sheet can produce global conformational changes. Examples include the appearance of spontaneous curvature due to strain variations across the thickness of the sheet [1–3] or non-Euclidean reference metrics induced by in-plane strain variations [4–8]. A theory of incompatible elastic plates [9,10] has been developed to determine equilibrium configurations of such sheets. Related approaches have been used to develop self-folding origami gels [11]. A catalog of responsive materials is now available for investigating the mechanics of thin sheets, including non-uniform responsive gel sheets [12–14], sheets of nematic elastomers with a non-uniform director field [15,16], responsive gels combined with oriented micro-rods [17], and sheets in confined geometries [18–21].

The *dynamics* of responsive gels were the focus of work by Yoshida and collaborators, who synthesized a gel that locally swells in response to chemical waves propagating entirely within the gel [22]. They used self-oscillating gels in various narrow strip geometries to make a variety of soft machines [23–27]. The Balazs group used poroelastic simulations of self-oscillating gels to demonstrate additional examples of soft machines with uniaxial bending or isotropic swelling [28–31]. Here we will focus on simulating the dynamics of an extensively-studied model, a thin elastic sheet driven by changes in its equilibrium metric. We will present an efficient semi-implicit time-stepping algorithm for the case of overdamped dynamics, a representative case with the same form of numerical stiffness as more detailed fluid-elastic and fluid-poroelastic models.

* Corresponding author.
E-mail address: alben@umich.edu (S. Alben).

https://doi.org/10.1016/j.jcp.2019.108952
0021-9991/

The approach is also useful in other applications where the dynamics of thin elastic sheets are important, such as the self-assembly of thin sheets under magnetic forces [32,33], and the rolling of actuated bilayers [34,35].

A related problem is simulating the dynamics of fluid membrane vesicles with surface tension [36]. Here a similar time-step constraint arises for bending forces, while the thin elastic sheets considered in the present work also have stiffness due to stretching forces. Like [36], we develop a semi-implicit time-stepping approach for computational efficiency, though our formulation differs due to the different mechanical forces.

In general, a semi-implicit (or implicit-explicit) time discretization writes some of the terms (typically those with the highest spatial derivatives) implicitly, to improve time-step constraints for stability [37–45]. The implicit terms are typically linear in the unknowns at the current time step, so they can be solved directly at each time step, avoiding some of the complication and computational expense of nonlinear iterative solvers (e.g. Newton-type methods) in fully implicit discretizations [46]. If the linearized implicit term is sufficiently large in comparison to the explicit terms, the semi-implicit method may be stable for a wide range of time steps. For nonlinear PDEs, a somewhat empirical approach to formulating schemes, based on analogies with time-stepping for simpler linear PDEs, is often necessary.

In this work we begin with Seung and Nelson's discretization of elastic sheets by bending and stretching springs on a triangular lattice [47]. We use the approach of [40,43] to split the stretching force into an implicit linear term corresponding to zero-rest-length springs, and a nonlinear remainder. The implicit stretching term is proportional to a discrete Laplacian matrix multiplying the current sheet position. To stabilize the bending force, we add an implicit bending term that is proportional to a discrete biharmonic matrix multiplying the current sheet position. The resulting method was found to be numerically stable for all time steps. To allow for general elastic constants, we formulate a finite-difference discretization of the elastic energy with the analogous semi-implicit approach. We validate and compare the methods on test problems with internal in-plane stretching forces (nontrivial equilibrium metrics) and study the effects of basic physical parameters on the sheets' dynamics.

2. Elastic sheet

We consider a thin sheet or bilayer that undergoes large time-dependent deformations due to internal forces (from a prescribed, time- and space-varying reference metric). We assume the sheet obeys linear (Hookean) elasticity, but that the midsurface (the set of points located midway through the sheet in the thickness direction) can be an arbitrary smooth time-dependent surface, so elastic forces depend nonlinearly on its position. The extension of the Kirchhoff-Love (and Föppl-von-Kármán) models of elastic plates to nonflat reference metrics and/or large deformations with smooth midsurfaces has been called the Koiter shell theory [48–50], or the theory of non-Euclidean plates [9,51] for reference metrics without a stress-free configuration. Here we mainly follow the latter's notation.

The elastic energy involves stretching and bending energy terms determined by the position of the body, $\mathbf{r}(\mathbf{x})$. Here $\mathbf{r}$ lies in $\mathbb{R}^3$, as does the material coordinate $\mathbf{x} = (x_1, x_2, x_3)$. In the classical situation, the sheet has a zero-energy flat state $\mathbf{r}(\mathbf{x}) = \mathbf{x}$, where x_3 lies in the interval $[-h/2, h/2]$ (h is the sheet thickness, much smaller than the other dimensions), and x_1 and x_2 lie in a planar region, the same for each x_3. For a small line of material $\Delta\mathbf{x} = \tilde{\mathbf{x}} - \mathbf{x}$ connecting two material points $\tilde{\mathbf{x}}$ and $\mathbf{x}$, its squared length on the undeformed surface is $dl^2 = \Delta x_i \Delta x_i$ (with summation over repeated indices). Denote the squared length on the deformed surface $\mathbf{r}(\mathbf{x})$ by dl'^2. Using the Taylor series of $\mathbf{r}(\mathbf{x})$ up to first derivatives we have

$$dl'^2 - dl^2 = 2\epsilon_{ij}\Delta x_i \Delta x_j. \tag{1}$$

Here ϵ_{ij} is the strain tensor,

$$\epsilon_{ij} = \frac{1}{2}\left(g_{ij} - \delta_{ij}\right), \tag{2}$$

where

$$g_{ij} = \frac{\partial r_k}{\partial x_i}\frac{\partial r_k}{\partial x_j} \tag{3}$$

is the deformed covariant metric tensor. For curved shells or active materials, the rest state may be curved and/or time-varying, in which case the reference metric, δ_{ij} in (2), becomes $\bar{g}_{ij}(\mathbf{x}, t)$, a time- and space-varying function determined for example by chemical activity [12,22,28]:

$$\epsilon_{ij} = \frac{1}{2}\left(g_{ij} - \bar{g}_{ij}(\mathbf{x}, t)\right). \tag{4}$$

The reference metric is assumed to take the form

$$\bar{g} = \begin{pmatrix} \bar{g}_{11} & \bar{g}_{12} & 0 \\ \bar{g}_{21} & \bar{g}_{22} & 0 \\ 0 & 0 & 1 \end{pmatrix} \tag{5}$$

with upper 2-by-2 reference metric $\bar{g}_{\alpha\beta}$. The dependence on out-of-plane components ($\bar{g}_{\alpha 3}, \bar{g}_{3\alpha}$) is trivial, so shearing though the plate thickness is not imposed and expansion/contraction in the thickness direction occurs only passively, due to the Poisson ratio effect. The components of the metric g_{i3} for $i = 1, 2, 3$ are determined by the Kirchhoff-Love assumptions of no shearing in planes through the thickness, and no stress in the thickness direction. The result is $g_{\alpha 3} = g_{3\alpha} = 0$ for $\alpha = 1, 2$, and $g_{33} = 1$ [9].

We may write the energy in terms of the midsurface deformation by expanding $g_{\alpha\beta}$ about the sheet midsurface $x_3 = 0$. We obtain, at leading order, its thickness-average $a_{\alpha\beta}$ and its thickness-gradient $2b_{\alpha\beta}$ [9]:

$$g_{\alpha\beta} = a_{\alpha\beta} - 2x_3 b_{\alpha\beta} + O(h^2). \tag{6}$$

Here $a_{\alpha\beta}$ is the upper 2-by-2 part of the metric tensor (3) evaluated at the sheet midsurface, $x_3 = 0$. The thickness-gradient is twice $b_{\alpha\beta}$, the second fundamental form

$$b_{\alpha\beta} = \frac{\partial^2 r_k}{\partial x_\alpha \partial x_\beta} n_k \tag{7}$$

also evaluated at the sheet midsurface, $x_3 = 0$, with n_k the components of the midsurface unit normal vector $\mathbf{n}$. For the reference metric $\bar{g}$, we write $\bar{a}$ and $\bar{b}$ for the corresponding terms in the expansion about the midsurface.

For an isotropic sheet with Young's modulus E and Poisson ratio ν, the elastic energy per unit volume is

$$w = \frac{1}{2} \bar{A}^{\alpha\beta\gamma\delta} \epsilon_{\alpha\beta} \epsilon_{\gamma\delta}, \tag{8}$$

a quadratic function of the in-plane components of the strain tensor in (4) with elasticity tensor

$$\bar{A}^{\alpha\beta\gamma\delta} = \frac{E}{1+\nu} \left(\frac{\nu}{1-\nu} \bar{g}^{\alpha\beta} \bar{g}^{\gamma\delta} + \bar{g}^{\alpha\gamma} \bar{g}^{\beta\delta} \right) \tag{9}$$

where $\bar{g}^{\alpha\beta}$, the contravariant reference metric, has the same entries as $\bar{g}_{\alpha\beta}^{-1}$. Integrating w over the sheet thickness h, the energy per unit midsurface area is

$$w_{2D} = \int_{-h/2}^{h/2} w dx_3 = w_s + w_b + h.o.t., \tag{10}$$

a sum of stretching energy per unit area

$$w_s = \frac{h}{8} A^{\alpha\beta\gamma\delta} \left(a_{\alpha\beta} - \bar{a}_{\alpha\beta} \right) \left(a_{\gamma\delta} - \bar{a}_{\gamma\delta} \right) \tag{11}$$

and bending energy per unit area

$$w_b = \frac{h^3}{24} A^{\alpha\beta\gamma\delta} \left(b_{\alpha\beta} - \bar{b}_{\alpha\beta} \right) \left(b_{\gamma\delta} - \bar{b}_{\gamma\delta} \right) \tag{12}$$

in terms of the midsurface elasticity tensor

$$A^{\alpha\beta\gamma\delta} = \frac{E}{1+\nu} \left(\frac{\nu}{1-\nu} \bar{a}^{\alpha\beta} \bar{a}^{\gamma\delta} + \bar{a}^{\alpha\gamma} \bar{a}^{\beta\delta} \right), \tag{13}$$

and higher order terms in h. The total elastic energy is, to leading order in h,

$$W = W_s + W_b\,, \quad W_s = \iint w_s \sqrt{|\bar{a}|} dx_1 dx_2\,, \quad W_b = \iint w_b \sqrt{|\bar{a}|} dx_1 dx_2. \tag{14}$$

W is a function of the midsurface reference metric $\bar{a}$ and the midsurface configuration, $\mathbf{r}(x_1, x_2, 0)$, through $a_{\alpha\beta}$ in w_s (11) and $b_{\alpha\beta}$ in w_b (12). These tensors depend on $\mathbf{r}$ through (3), (6), and (7).

3. Sheet dynamics

The sheet midplane evolves according a force balance equation, where the elastic force per unit area $\mathbf{f}$ acting at a point on the midplane is a sum of stretching and bending forces per unit area:

$$\mathbf{f} = \mathbf{f}_s + \mathbf{f}_b = \delta w_s / \delta \mathbf{r} + \delta w_b / \delta \mathbf{r} \tag{15}$$

given by taking the variation of $w_s + w_b$ with respect to $\mathbf{r}$. For a sheet moving in Stokes flow (i.e. at zero Reynolds number) the elastic forces would be balanced by external fluid forces which depend linearly on the sheet velocity [36]:

$$\frac{\partial \mathbf{r}}{\partial t} = \mathcal{S}[\mathbf{f}_s + \mathbf{f}_b](\mathbf{r}), \tag{16}$$

where $\mathcal{S}$ is the Stokes operator

$$\mathcal{S}[\mathbf{f}](\mathbf{r}) = \int G(\mathbf{r}, \mathbf{r}')\mathbf{f}(\mathbf{r}')dA(\mathbf{r}'), \quad G(\mathbf{r}, \mathbf{r}') = \frac{1}{8\pi\mu}\left(\frac{1}{\|\rho\|}\mathbf{I} + \frac{\rho \otimes \rho}{\|\rho\|^3}\right), \quad \rho \equiv \mathbf{r} - \mathbf{r}'. \tag{17}$$

In this work, we consider a simplification of (16) which has similar numerical stiffness issues: overdamped dynamics, in which the Stokes operator is replaced with a multiple of the identity:

$$\mu\frac{\partial \mathbf{r}}{\partial t} = \mathbf{f}. \tag{18}$$

Here μ is a parameter that can be used to model the effects of internal and external damping. The equation can also be used to identify equilibria as a gradient descent method [52] with time playing a nonphysical role. Extensions of (18) including the inertia of the sheet or a surrounding fluid would add a dependence on $\partial^2\mathbf{r}/\partial t^2$. When discretized, the Δt^{-2} dependence of such terms will improve the time-step constraint compared to the overdamped problem, for explicit schemes [53]. In this work, we develop a semi-implicit approach for (18), which should also apply with more detailed forms of internal and external damping/forcing, e.g. from a fluid. In the subsequent computational results we nondimensionalize the sheet lengths by the radius or half-width R (e.g. for hexagonal and square sheets), energy by the bending energy scale $Eh^3/12$, and time by the period of $\bar{g}_{\alpha\beta}(\mathbf{x}, t)$ (assumed to be time-periodic). These choices define dimensionless versions of all the parameters (e.g. μ).

4. Triangular lattice with stretching and bending springs

We first consider a simple model of an elastic sheet with material points connected by an equilateral triangular lattice mesh. Nearest neighbor points are connected by Hookean springs and the total stretching energy is proportional to the sum of the squares of nearest neighbor distances minus the local spring rest length d_{ij}:

$$U_s = \frac{K_s}{2}\sum_{i,j}(\|\mathbf{r}_i - \mathbf{r}_j\| - d_{ij})^2, \tag{19}$$

with K_s a stretching stiffness constant. A bending energy is applied to adjacent triangular faces based on the angles between the normals to the faces. The total bending energy is a sum over nearest neighbor pairs multiplied by a bending stiffness constant K_b:

$$U_b = \frac{K_b}{2}\sum_{k,l}\|\mathbf{n}_k - \mathbf{n}_l\|^2 = K_b\sum_{k,l}1 - \mathbf{n}_k \cdot \mathbf{n}_l. \tag{20}$$

Seung and Nelson used this model to study buckling due to defects in elastic membranes [47], and it was used by many other groups to study other deformations of thin sheets and shells due to defects and/or external forces [35,54–61], as well as polymerized and fluid membranes [62].

Seung and Nelson showed that for a lattice with $d_{ij} \equiv d$, a constant, as d tends to 0 the stretching energy U_s tends to that of an isotropic thin sheet with stretching rigidity $Eh = 2K_s/\sqrt{3}$ and Poisson ratio $\nu = 1/3$. The continuum limit of the bending energy contains two terms, one proportional to the mean curvature squared and the other proportional to the Gaussian curvature. The term involving mean curvature tends to that of an isotropic thin sheet with bending rigidity $Eh^3/12(1-\nu^2) = \sqrt{3}K_b/2$. However, with this bending rigidity, the prefactor of the Gaussian curvature term is too large for $\nu > -1/3$ (too large by a factor of two at $\nu = 1/3$) [63]. Nonetheless, for many problems, the Gaussian curvature term plays a negligible role because it can be integrated to yield only boundary terms. For closed shells, the Gaussian curvature term integrates to a constant and thus does not affect the elastic forces [56]. For open sheets (with boundaries), the equilibrium shape could be insensitive to the boundary shape or boundary conditions, particularly if the external or internal actuation is not localized at the boundary. In this work we will compare the model to a finite-difference discretization with $\nu = 1/3$ in two cases, and find a very small difference in a case of static actuation (also found in another situation by [64]), and a somewhat larger difference in a case of dynamic actuation.

The triangular lattice sheet is useful computationally because it has a simple expression for the energy and motivates our semi-implicit approach for the more general finite difference discretization given subsequently. The elastic force on the triangular lattice is obtained by taking gradients of (19) and (20) with respect to vertex coordinates $\{\mathbf{r}_i\}$. The gradient of (19) with respect to $\mathbf{r}_i$ is

$$\nabla_{\mathbf{r}_i}U_s = K_s\sum_{j\in\text{nhbrs}(i)}(\|\mathbf{r}_i - \mathbf{r}_j\| - d_{ij})\frac{(\mathbf{r}_i - \mathbf{r}_j)}{\|\mathbf{r}_i - \mathbf{r}_j\|}, \tag{21}$$

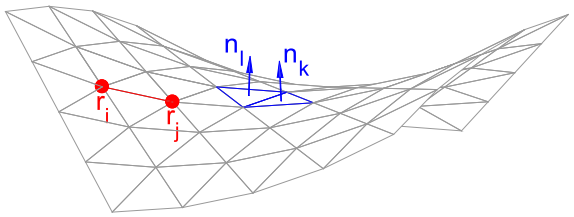

Fig. 1. Triangular lattice mesh with examples of elements in the elastic energy: adjacent vertices $\mathbf{r}_i$ and $\mathbf{r}_j$ (red) and adjacent face normals $\mathbf{n}_k$ and $\mathbf{n}_l$ (blue). (For interpretation of the colors in the figure(s), the reader is referred to the web version of this article.)

where nhbrs(i) is the set of vertex neighbors to i. Following [40,43] we write the summand as a linear term plus a term with constant magnitude,

$$\nabla_{\mathbf{r}_i} U_s = K_s \sum_{j\in\text{nhbrs}(i)} \mathbf{r}_i - \mathbf{r}_j - d_{ij}\frac{(\mathbf{r}_i-\mathbf{r}_j)}{\|\mathbf{r}_i-\mathbf{r}_j\|}. \tag{22}$$

To write the algorithms we define

$$\boldsymbol{r} = \left[\boldsymbol{r}_x^\mathsf{T}, \boldsymbol{r}_y^\mathsf{T}, \boldsymbol{r}_z^\mathsf{T}\right]^\mathsf{T} \tag{23}$$

as the vector of $3N$ vertex coordinates, with $\boldsymbol{r}_x$, $\boldsymbol{r}_y$, and $\boldsymbol{r}_z$ the N-vectors of x-, y-, and z-coordinates. Thus $\mathbf{r}_i = \left[(\boldsymbol{r}_x)_i, (\boldsymbol{r}_y)_i, (\boldsymbol{r}_z)_i\right]^\mathsf{T}$. Also note that the italicized $\boldsymbol{r}\in\mathbb{R}^{3N}$ is different from the position function $\mathbf{r}(\mathbf{x})$ and a vertex on the discretized surface $\mathbf{r}_i$, both of which take values in $\mathbb{R}^3$. It turns out that the linear term in (22) can be written as the product of K_s and a block diagonal matrix $\mathbf{L}$ with $\boldsymbol{r}$, where $\mathbf{L}$ has three blocks (along the diagonal), each of which is a discretized Laplacian on the triangular mesh with free-edge boundary conditions (see examples of stencils in Fig. 2, top row), a negative semidefinite matrix. Each block multiplies $\boldsymbol{r}_x$, $\boldsymbol{r}_y$, and $\boldsymbol{r}_z$, respectively. We treat the linear term implicitly and the constant-magnitude term explicitly. Collecting the terms (22) for all vertices i, we obtain the total stretching force. A semi-implicit first-order temporal discretization of (18) with stretching forces only is:

$$\mu A_p \frac{\boldsymbol{r}^{n+1}-\boldsymbol{r}^n}{\Delta t} = K_s\mathbf{L}\boldsymbol{r}^{n+1} + \mathbf{f}_{SE}(\boldsymbol{r}^n), \quad [\mathbf{f}_{SE}(\boldsymbol{r})_i, \mathbf{f}_{SE}(\boldsymbol{r})_{N+i}, \mathbf{f}_{SE}(\boldsymbol{r})_{2N+i}]^\mathsf{T} \equiv -K_s \sum_{j\in\text{nhbrs}(i)} d_{ij}\frac{(\mathbf{r}_i-\mathbf{r}_j)}{\|\mathbf{r}_i-\mathbf{r}_j\|}. \tag{24}$$

Here $A_p = n_p\sqrt{3}d^2/12$ is the area per point on the undeformed lattice, with n_p the number of triangles of which the point is a vertex, 6 for interior points and fewer for boundary points. $\mathbf{f}_{SE}(\boldsymbol{r})$ is the nonlinear term in (22), with $3N$ entries, given on the right side of (24) for $i = 1,\ldots,N$.

Now assume the spring rest lengths are bounded for all time: $d_{ij}\le\bar{d}$, a constant, and each vertex has at most p neighbors (6 for the triangular lattice). Rearranging (24) and using the boundedness of $\mathbf{f}_{SE}(\boldsymbol{r})$, we have an upper bound at time step $n+1$:

$$\left\|\boldsymbol{r}^{n+1}\right\| \le \left\|(\mathbf{I}-\Delta t K_s\mathbf{L}/(\mu A_p))^{-1}\boldsymbol{r}^n\right\| + \left\|(\mathbf{I}-\Delta t K_s\mathbf{L}/(\mu A_p))^{-1}\mathbf{f}_{SE}(\boldsymbol{r}^n)\right\| \tag{25}$$

$$\le \left\|\boldsymbol{r}^n\right\| + K_s p\bar{d} \tag{26}$$

$$\le \left\|\boldsymbol{r}^0\right\| + (n+1)K_s p\bar{d}. \tag{27}$$

So $\|\boldsymbol{r}^{n+1}\|$ grows at most linearly in time with this discretization. Empirically, the iteration appears to be bounded for all time steps for spring rest lengths d_{ij} that are bounded in time. For comparison, a forward Euler discretization of (18) with stretching forces only results in

$$\boldsymbol{r}^{n+1} = \left(\mathbf{I}+\Delta t K_s\mathbf{L}/(\mu A_p)\right)\boldsymbol{r}^n + \frac{\Delta t}{\mu A_p}\mathbf{f}_{SE}(\boldsymbol{r}^n). \tag{28}$$

Neglecting the rightmost term in (28), we have a 2D diffusion equation, and stability is possible only when the largest eigenvalue of $\mathbf{I}+\Delta t K_s\mathbf{L}/(\mu A_p)$ is bounded in magnitude by 1. Since the eigenvalues of $\mathbf{L}\sim 1/\Delta x^2$ for lattice spacing Δx, this requires $\Delta t < C_s\mu A_p\Delta x^2/K_s$ for a constant C_s.

The gradient of the bending energy (20) with respect to a lattice vertex $\mathbf{r}_i$ is

$$\nabla_{\mathbf{r}_i} U_b = K_b\sum_{k,l}\sin\theta_{kl}\nabla_{\mathbf{r}_i}\theta_{kl}, \tag{29}$$

using $\mathbf{n}_k\cdot\mathbf{n}_l = \cos\theta_{kl}$. The dihedral angle θ_{kl} depends on the four points in the union of the neighboring triangles k and l (see Fig. 1). Two of these points are the endpoints of the edge shared by the triangles. At each of the other two points,

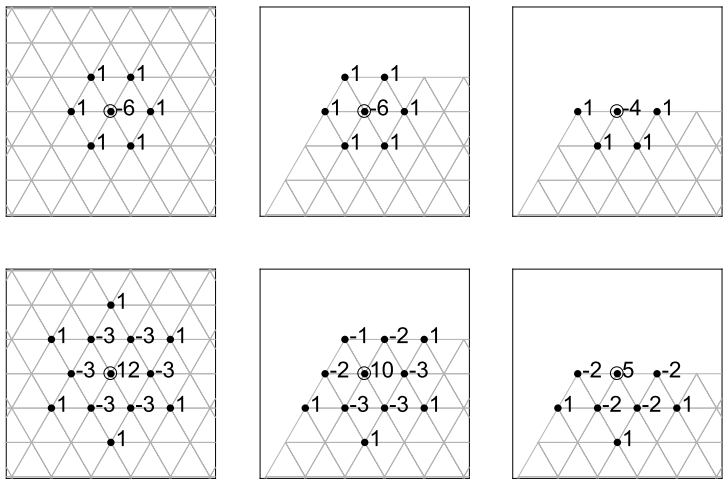

Fig. 2. Examples of the stencils corresponding to a discrete Laplacian operator with free edge boundary conditions (one of the diagonal blocks of $\mathbf{L}$ defined below (22)) (top row), and $\tilde{\Delta}^2_{x_1,x_2}$, a discrete biharmonic operator with free edge boundary conditions (bottom row), at different mesh points (circled) away from and near a boundary on the triangular lattice.

$\nabla_{\mathbf{r}_i}\theta_{kl}$ is directed along the normal to the triangle in which it lies, with magnitude equal to the reciprocal of its distance from the shared edge. At the endpoints of the shared edge, $\nabla_{\mathbf{r}_i}\theta_{kl}$ can be found by requiring that the net force and torque due to θ_{kl} is zero, which gives six equations (for the three components of net force and torque) in six unknowns (the forces on the two endpoints of the shared edge). The bending force $\mathbf{f}_B$ is a $3N$-vector with components

$$[\mathbf{f}_B(\boldsymbol{r})_i, \mathbf{f}_B(\boldsymbol{r})_{N+i}, \mathbf{f}_B(\boldsymbol{r})_{2N+i}]^{\mathsf{T}} \equiv -\nabla_{\mathbf{r}_i} U_b,\ i = 1, \ldots, N, \tag{30}$$

similar to $\mathbf{f}_{SE}$ in (24). Our linearized approximation to the bending force is similar to that of [36]. They write the terms with the highest spatial derivatives in the form $\mathcal{B}(\boldsymbol{r}^n)\boldsymbol{r}^{n+1}$. Here $\mathcal{B}$ involves fourth derivatives with prefactors that include lower-order derivatives extrapolated to time step $n+1$ from previous time steps. In fact, we use a simpler expression: $\mathbf{B}\boldsymbol{r}^{n+1}$, where $\mathbf{B}$ is a block diagonal matrix with each of the three blocks equal to $D\tilde{\Delta}^2_{x_1,x_2}$. Here D is the bending modulus ($Eh^3/(12(1-\nu^2))$ in dimensional form, $1/(1-\nu^2)$ in dimensionless form) and $\tilde{\Delta}^2_{x_1,x_2}$ is the discretized biharmonic operator on the triangular lattice in the orthogonal material coordinates x_1 and x_2. If in-plane strain (shearing and dilation) is not very large, x_1 and x_2 are close to orthogonal arclength coordinates s_1 and s_2 along the midplane surface. For any surface $\mathbf{X}(s_1, s_2)$ parametrized by orthogonal arclength coordinates s_1 and s_2 we can write

$$\Delta^2_{s_1,s_2}\mathbf{X}(s_1, s_2) = \Delta_{s_1,s_2}(\kappa_1 + \kappa_2)\hat{\mathbf{n}} + N, \tag{31}$$

where $\kappa_1 + \kappa_2$ is twice the mean curvature and $N = 2(\nabla_{s_1,s_2}(\kappa_1 + \kappa_2) \cdot \nabla_{s_1,s_2})\hat{\mathbf{n}} + (\kappa_1 + \kappa_2)\Delta_{s_1,s_2}\hat{\mathbf{n}}$ involves derivatives of $\mathbf{X}$ that are of lower order than those in the first term on the right hand side. The highest-derivative term in the continuum bending force is also the first term on the right hand side of (31) when the equilibrium metric is the identity (see [36,65]). Thus the left hand side of (31) is a reasonable linear (and constant-coefficient) approximation to the bending force. A more accurate linear approximation to the bending operator could include corrections that take into account the nontrivial inverse equilibrium metric ($\bar{g}^{\alpha\beta}$ in (13)) and in-plane strain, e.g. by including nonuniform prefactors extrapolated from previous time steps. We find however that the constant-coefficient biharmonic is a sufficiently good approximation in the sense that it damps out spurious mesh-scale bending oscillations (as occurs with a fully explicit bending term) up to large-amplitude variations in the reference metric, ≈ 0.3 in terms of an amplitude parameter A defined in (34)–(36), below. With larger variations in the reference metric, the position vector remains bounded in time, but there is very large deformation and self-intersection even for the case of purely planar deformations, without bending forces. We explain how the discrete biharmonic operator $\tilde{\Delta}^2_{x_1,x_2}$ is calculated in appendix A.

Semi-implicit (or implicit-explicit) schemes for cloth animation have sometimes left bending forces explicit, when they are much smaller than stretching forces [41]. Considering a forward Euler discretization of (18) with bending forces only, and approximating the bending force by $\mathbf{B}\boldsymbol{r}^n$, stability requires $\Delta t < C_b \mu A_p \Delta x^4/K_b$ for a constant C_b, since the eigenvalues of $\mathbf{B} \sim 1/\Delta x^4$ for lattice spacing Δx. The ratio of bending to stretching time step constraints $\sim K_s\Delta x^2/K_b \sim \Delta x^2/h^2$, the square of the ratio of lattice spacing to sheet thickness. For the parameters used in this work, the stretching and bending time step constraints are comparable, so a semi-implicit approach needs to address both terms.

Our first-order semi-implicit discretization for sheet dynamics with both stretching and bending forces is:

$$\mu A_p \frac{\boldsymbol{r}^{n+1} - \boldsymbol{r}^n}{\Delta t} = K_s \mathbf{L}\boldsymbol{r}^{n+1} + \mathbf{f}_{SE}(\boldsymbol{r}^n) + \mathbf{B}\boldsymbol{r}^{n+1} - \mathbf{B}\boldsymbol{r}^n + \mathbf{f}_B(\boldsymbol{r}^n). \tag{32}$$

The last two terms on the right hand side approximately cancel in the highest-derivative term, leaving the implicit bending term $\mathbf{B}\boldsymbol{r}^{n+1}$ as the dominant one. The second-order version with uniform time stepping (an approximate backward differentiation formula) is:

$$\mu A_p \frac{3\boldsymbol{r}^{n+1} - 4\boldsymbol{r}^n + \boldsymbol{r}^{n-1}}{2\Delta t} = K_s \mathbf{L}\boldsymbol{r}^{n+1} + 2\mathbf{f}_{SE}(\boldsymbol{r}^n) - \mathbf{f}_{SE}(\boldsymbol{r}^{n-1}) + \mathbf{B}\boldsymbol{r}^{n+1} - 2\mathbf{B}\boldsymbol{r}^n + \mathbf{B}\boldsymbol{r}^{n-1} + 2\mathbf{f}_B(\boldsymbol{r}^n) - \mathbf{f}_B(\boldsymbol{r}^{n-1}). \quad (33)$$

For test problems that model the deformation and dynamics of active gel sheets driven by internal swelling [12,22,28,30], we construct a uniform triangular lattice with spacing d. We then set the dilatation factor $d_{ij}/d \equiv \eta$ to correspond to one of three examples: a static radial distribution, a unidirectional traveling wave, or a radial traveling wave of isotropic dilation/contraction:

$$\eta_1(x_1, x_2) = 1 + A \sin\left(2\pi\left(k\sqrt{x_1^2 + x_2^2}\right)\right) \quad (34)$$

$$\eta_2(x_1, x_2, t) = 1 + A \sin\left(2\pi\left(kx_1 - t\right)\right) \quad (35)$$

$$\eta_3(x_1, x_2, t) = 1 + A \sin\left(2\pi\left(k\sqrt{x_1^2 + x_2^2} - t\right)\right). \quad (36)$$

The corresponding equilibrium metrics are

$$\bar{a}_{\alpha\beta}(x_1, x_2, t) = \eta^2(x_1, x_2, t)\delta_{\alpha\beta}, \quad (37)$$

and we take zero reference curvature ($\bar{b}_{\alpha\beta} = 0$) for simplicity. Before presenting results, we describe in the next section a more direct finite difference simulation that allows for more general elastic parameters than the triangular lattice model. However, the triangular lattice simulations have the advantage of remaining bounded in time for all time steps across wide ranges (several orders of magnitude) of values for the parameters (h, A, k, μ) with large mesh sizes (hexagonal domains with N up to 58145, for example). Simulations appear smooth up to strain amplitudes $A \sim 0.3$. Above this value, sheet shapes become jagged and self-intersect, but remain bounded in time. Hence the time step and lattice spacing are constrained only by the need to resolve the dynamics at a given parameter set. The method can also be used to converge to static equilibria, in which case the time step becomes a step length for a gradient descent algorithm. Here a large step length may be used initially to rapidly approach the neighborhood of an equilibrium, and then a smaller step length allows for convergence. The resulting convergence is geometric (not superlinear) but generally quite fast, and due to the simplicity of the formulation it is a good alternative to Newton and quasi-Newton methods in the static case (as well as the dynamic case).

5. Finite difference algorithm

We now propose a second algorithm, inspired by that for the triangular lattice, but based on a finite difference discretization of the continuum elastic energy (14), and which therefore allows the full range of values of E, h, and ν (that are physically reasonable). We use a square grid with grid spacing Δx for simplicity and define second-order accurate finite-difference operators:

$$D_\alpha \approx \partial_\alpha\ ,\ D_{\alpha\beta} \approx \partial^2_{\alpha\beta}\ ,\ \alpha, \beta = \{1, 2\} \quad (38)$$

In the energy (14) we use

$$a_{\alpha\beta} \approx D_\alpha \boldsymbol{r}_x \odot D_\beta \boldsymbol{r}_x + D_\alpha \boldsymbol{r}_y \odot D_\beta \boldsymbol{r}_y + D_\alpha \boldsymbol{r}_z \odot D_\beta \boldsymbol{r}_z, \quad (39)$$

where $\odot$ denotes a componentwise (Hadamard) product of two vectors. We use the analogous expression for $b_{\alpha\beta}$ and a trapezoidal-rule quadrature for the integrals in (14). For equilibrium metrics in the form (37) the discrete form of the stretching energy (W_s in (14)) is

$$\tilde{W}_s = \frac{h}{8} A^{\alpha\beta\gamma\delta} \left(\mathbf{q} \odot \eta^2\right)^{\mathsf{T}} \left[\left(a_{\alpha\beta} - \bar{a}_{\alpha\beta}\right) \odot \left(a_{\gamma\delta} - \bar{a}_{\gamma\delta}\right)\right] \quad (40)$$

where $\mathbf{q}$ is the vector of quadrature weights for the trapezoidal rule on the rectangular mesh, and we use the usual summation rule for repeated indices. We compute $\nabla_{\boldsymbol{r}_x} \tilde{W}_s$ by using the chain rule with (39) and (40):

$$\nabla_{\boldsymbol{r}_x} \tilde{W}_s = \frac{h}{4} D_\alpha^{\mathsf{T}} \left[A^{\alpha\beta\gamma\delta} \left(\mathbf{q} \odot \eta^2 \odot \left(a_{\gamma\delta} - \bar{a}_{\gamma\delta}\right)\right) D_\beta \boldsymbol{r}_x)\right] + \frac{h}{4} D_\beta^{\mathsf{T}} \left[A^{\alpha\beta\gamma\delta} \left(\mathbf{q} \odot \eta^2 \odot \left(a_{\gamma\delta} - \bar{a}_{\gamma\delta}\right)\right) D_\alpha \boldsymbol{r}_x)\right] \quad (41)$$

and the same expressions for $\nabla_{\boldsymbol{r}_y} \tilde{W}_s$ and $\nabla_{\boldsymbol{r}_z} \tilde{W}_s$, with $\boldsymbol{r}_x$ in (41) replaced by $\boldsymbol{r}_y$ and $\boldsymbol{r}_z$ respectively. Our linearized approximation to the stretching force, to compute $\boldsymbol{r}^{n+1}$ semi-implicitly, is $\mathbf{M}_s^n \boldsymbol{r}^{n+1}$, where $\mathbf{M}_s^n$ is a block diagonal matrix with three blocks, each given by

Table 1
Approximate upper bounds on stable time step for the semi-implicit finite difference scheme (SI) compared to forward Euler (FE), for simulations on a square of side length 2 with different mesh spacings d_{FD}.

d_{FD}	Δt^{SI}_{max}	Δt^{FE}_{max}
1/16	0.04	1.8×10^{-4}
1/22	0.03	1.0×10^{-4}
1/27	0.025	5×10^{-5}
1/32	0.02	3×10^{-5}

$$\frac{h}{4} D_\alpha^\intercal \left[A^{\alpha\beta\gamma\delta} \left(\mathbf{q} \odot \eta^2 \odot a^n_{\gamma\delta} \right) D_\beta) \right] + \frac{h}{4} D_\beta^\intercal \left[A^{\alpha\beta\gamma\delta} \left(\mathbf{q} \odot \eta^2 \odot a^n_{\gamma\delta} \right) D_\alpha) \right]. \tag{42}$$

$\mathbf{M}_s^n \boldsymbol{r}^{n+1}$ is the discrete stretching force with zero reference metric, analogous to the discrete Laplacian on the triangular lattice, which gives the stretching force with zero-rest-length springs. The use of $a^n_{\gamma\delta}$ instead of $a^{n+1}_{\gamma\delta}$ makes $\mathbf{M}_s^n$ independent of $\boldsymbol{r}^{n+1}$. An extrapolation that is higher-order in time can also be used.

We also compute $\nabla_{\boldsymbol{r}} W_b$ using the chain rule, resulting in a similar (though somewhat lengthier) expression for the bending force. Our linearized approximation to the bending force is $\mathbf{M}_b \boldsymbol{r}^{n+1}$, where $\mathbf{M}_b$ is the product of the bending modulus and the discrete biharmonic operator, the same as for the triangular lattice but now on a rectangular mesh.

Unlike the triangular lattice algorithm, the finite difference algorithm is only stable for first-order time-stepping, i.e.

$$\mu A_p \frac{\boldsymbol{r}^{n+1} - \boldsymbol{r}^n}{\Delta t} = \mathbf{M}_s^n \boldsymbol{r}^{n+1} - \mathbf{M}_s^n \boldsymbol{r}^n - \left\{ \nabla_{\boldsymbol{r}} \tilde{W}_s \right\}^n + \mathbf{M}_b \boldsymbol{r}^{n+1} - \mathbf{M}_b \boldsymbol{r}^n - \left\{ \nabla_{\boldsymbol{r}} \tilde{W}_b \right\}^n, \tag{43}$$

the analogue of (32), with $A_p = \Delta x^2$ the area per point (multiplied by 1/2 at points along the sides and 1/4 at the corners). It is unstable for the second-order version,

$$\mu A_p \frac{3\boldsymbol{r}^{n+1} - 4\boldsymbol{r}^n + \boldsymbol{r}^{n-1}}{2\Delta t} = \mathbf{M}_s^{[n+1]} \boldsymbol{r}^{n+1} - 2\mathbf{M}_s^{[n]} \boldsymbol{r}^n + \mathbf{M}_s^{[n-1]} \boldsymbol{r}^{n-1} - 2 \left\{ \nabla_{\boldsymbol{r}} \tilde{W}_s \right\}^n + \left\{ \nabla_{\boldsymbol{r}} \tilde{W}_s \right\}^{n-1} \tag{44}$$

$$+ \mathbf{M}_b \boldsymbol{r}^{n+1} - 2\mathbf{M}_b \boldsymbol{r}^n + \mathbf{M}_b \boldsymbol{r}^{n-1} - 2 \left\{ \nabla_{\boldsymbol{r}} \tilde{W}_b \right\}^n + \left\{ \nabla_{\boldsymbol{r}} \tilde{W}_b \right\}^{n-1} \tag{45}$$

due to the extrapolated gradient terms (i.e. (44)–(45) becomes stable when the extrapolation reverts to first order for the gradient terms in (45)). The superscripts in brackets denote a second-order extrapolation to the indicated time step using the two preceding time steps. We note that second-order accuracy can be obtained from the first order method via Richardson extrapolation.

While the triangular lattice algorithm is essentially unconditionally stable, the first-order finite-difference algorithm is only stable up to moderately large time steps. However, the semi-implicit operators do yield orders-of-magnitude improvements in the largest stable time steps compared to an explicit scheme (forward Euler). As an example, we set $\eta = \eta_3$ in (36), with $A = 0.1$, $h = 0.03$, $\mu = 1000$, and $\nu = 1/3$. In Table 1 we give approximate values for the maximum stable time step, defined to be a time step such that the sheet deflection remains bounded (below 10^8 in maximum norm) up to $t = 5$. The sheet is a square of side length 2, with a square grid of mesh spacing d_{FD}. As d_{FD} is decreased from 1/16 to 1/32, the maximum stable time step decreases by a factor of 2 for the semi-implicit method, versus a factor of 6 for the explicit method. Because the cost of solving the linear systems in (32), (33), and (43) is only slightly larger than the cost of the rest of the algorithm for the smallest d_{FD} in Table 1, the orders-of-magnitude difference in time step translates to an orders-of-magnitude difference in overall computational cost for these mesh sizes.

6. Results

We now present a sequence of simulation results to display basic aspects of the algorithms and parameters. First, we compare the triangular lattice and finite difference methods in two situations. The first is the equilibrium sheet deformation with a nontrivial, but static (time-independent) reference metric given by $\eta = \eta_1$ in (34), with $A = 0.1$, $k = 1$, $h = 0.03$, $\mu = 1000$, and $\nu = 1/3$. The sheets are initially nearly flat squares ($z = 0.02(x_1^4 + x_2^4)$, $-1 \le x_1 = x, x_2 = y \le 1$), and rapidly buckle into the shapes shown in Fig. 3. Three sheets are shown in oblique view (top row) and side view (bottom row). The leftmost sheet is computed with the triangular lattice algorithm, with jagged edges along one pair of sides. The center sheet is the result of the finite difference algorithm, with a different Poisson ratio value in one of the bending energy terms, to match those of the triangular lattice algorithm. For equilibrium metrics (37) we may write (12) as

$$w_b = \frac{Eh^3}{24(1-\nu^2)} \eta^4 \left((b_{11} + b_{22})^2 - 2(1 - \nu_B)(b_{11} b_{22} - b_{12}^2) \right). \tag{46}$$

In the stretching energy term (11) and the prefactor of the right hand side of (46), we set $\nu = 1/3$. We have denoted the second appearance of ν in (46) as ν_B (within $1 - \nu_B$) on the right hand side of (46). For the center sheet, we set $\nu = 1/3$

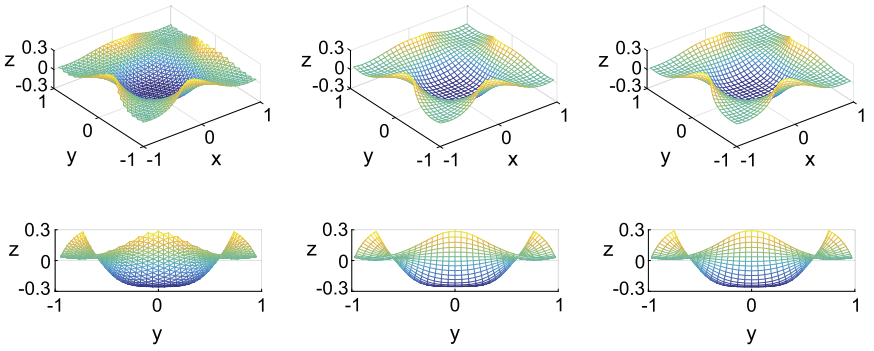

Fig. 3. A static equilibrium for the triangular lattice algorithm (left), and the finite difference algorithms with different Poisson ratios in one of the bending energy terms (center and right). The reference metric is $\eta = \eta_1$ in (34), with physical parameters $A = 0.1$, $k = 1$, $h = 0.03$, $\mu = 1000$. The Poisson ratio ν is 1/3 in the stretching energy term in all three cases. The leftmost plot has $\nu_B = -1/3$ in the $(1 - \nu_B)$ term in the bending energy (46), a consequence of the lattice model. The center plot also has $\nu_B = -1/3$ in the $(1 - \nu_B)$ term in the bending energy (46), but with a finite difference model. The rightmost plot has $\nu_B = \nu = 1/3$ instead, a fully consistent value.

but ν_B to -1/3, giving an elastic energy consistent with that of the triangular lattice model according to [63]. The rightmost sheet is also given by the finite difference algorithm but with $\nu = \nu_B = 1/3$ in all stretching and bending energy terms. The deformations are very close in all three cases. The differences between maximum and minimum z values, Δz, are within 1% for the center and leftmost sheets, and the difference is about 2% for the center and rightmost sheets. In this case at least, the error in Gaussian bending rigidity in the triangular lattice algorithm has only a modest effect, as was found by [64] in a different problem.

In Fig. 4 we present another equilibrium shape for the same static reference metric ($\eta = \eta_1$ in (34)) and the same three models as in Fig. 3. This shape is found by starting from a different initial deformation: $z = 0.3(2x_1^2 - 1)$, $-1 \le x_1 = x, x_2 = y \le 1$. The top two rows show good visual agreement between all three models in this second example, this time with finer meshes: $d_{TL} = 1/112$ for the triangular lattice (left) and $d_{FD} = 1/48$ for the finite difference models (center and right). In the third row, we show the convergence to the equilibria over time for the three models, measured by the decay of the energy gradient norm $\|\nabla W\|$. The convergence is fastest for the triangle lattice model (third row, left), but all the algorithms have a similar behavior: an initially rapid decay followed by a slower, but still exponential, decay. The fourth row shows the convergence of the total deflection Δz to its equilibrium values, for various mesh spacings. The temporal convergence is again slower for the finite difference models, while the convergence with mesh refinement is somewhat faster, probably because the finite difference models are second-order in space, while the triangular lattice mesh matches the square boundary only to first-order accuracy due to the jagged edges.

Table 2 shows the equilibrium values of Δz for various mesh spacings for the three models. The convergence with mesh refinement is generally somewhat faster for the finite difference models. Unlike the case in Fig. 3, here the values of the triangular lattice Δz (second column) are closest to those of the finite difference model with $\nu_B = 1/3$, shown in the fifth column. This is somewhat surprising because the case with $\nu_B = -1/3$ matches the continuum energy of the triangular lattice model [63]. We propose a few possible reasons for the discrepancies among the values of Δz in the three models. First, the triangular lattice model of the square has a jagged boundary. Although its position converges (at first order in lattice spacing) to the straight boundary assumed in the finite difference algorithm, its tangent angle does not, which may cause a small persistent different with the finite difference models. Second, there is the aforementioned difference in the Poisson ratio in one of the bending terms of the triangular lattice model [63], though accounting for this in the finite difference model (fourth column of Table 2) increases the discrepancy in Δz for the equilibrium in Fig. 4 and Table 2. Reference [63] also notes that at large deformations, the resistance to shear in the triangular lattice algorithm differs slightly from that of a continuum isotropic elastic sheet, a third possible reason for the discrepancy.

We now consider an unsteady reference metric, $\eta = \eta_2$ in (35), a unidirectional traveling wave, in both algorithms. We again take square sheets, with the same spatial grids and initial conditions as before, with (smaller) $A = 0.03$, $k = 1$, $h = 0.03$, $\mu = 1000$, and $\nu_B = \nu = 1/3$ only now, i.e. a single finite difference algorithm, for simplicity. The time step $\Delta t = 0.005$. Fig. 5 compares the dynamics. Panels A and B show Δz versus time for the triangular lattice and finite difference algorithms, respectively at three mesh spacings (labeled). For both algorithms the solutions have a strong oscillatory component with the same frequency as the reference metric, as one would expect. The solutions have other components that evolve on much longer time scales (tens to hundreds of periods), and even with modest deflections (here, about 7% of the square side length), the solutions can evolve in complicated ways over long time scales. The dynamics of Δz are qualitatively similar, though the peaks and troughs are about 10-15% larger for the finite difference algorithm. The spatial distribution of z deflection at $t = 31.5$ and 32 is shown in panels C and E for the triangular lattice algorithm and D and F for the finite difference algorithm, respectively. The distribution of deflection is very similar in both algorithms. We believe the reasons for the discrepancies are similar to those for the static cases already mentioned: the Poisson ratio in one of the bending terms ν_B is different in the continuum limits of the two models in Fig. 5, the triangular lattice has a jagged boundary, and responds slightly differently to shear at large deformations [63].

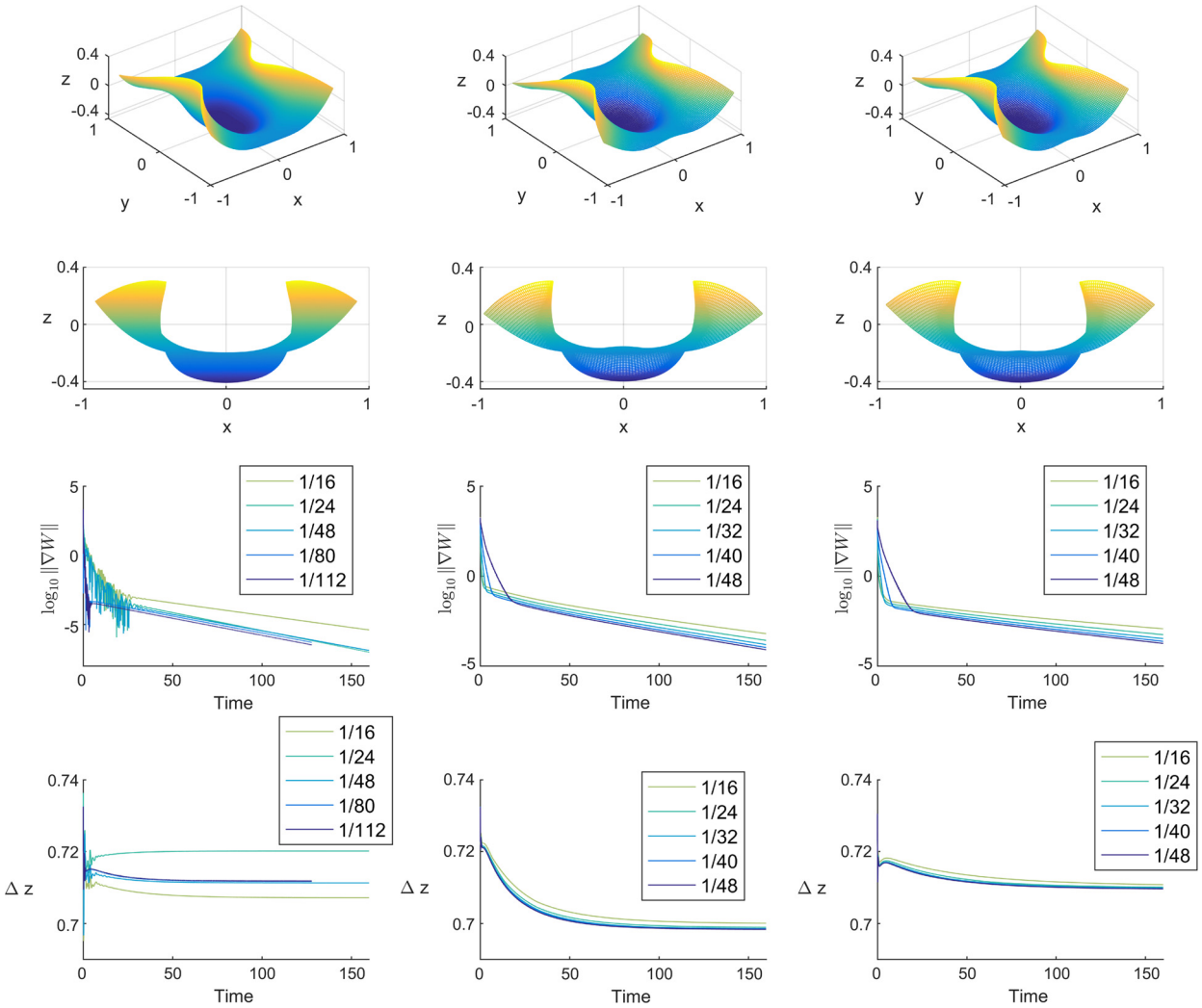

Fig. 4. A second static equilibrium for the reference metric $\eta = \eta_1$ in (34), computed with the triangular lattice algorithm (left), and the finite difference algorithms with different Poisson ratios in one of the bending energy terms (center and right). The physical parameters are the same as in Fig. 3 but finer meshes are used. The top two rows show oblique and side views of the equilibrium. The third row shows the decay of the energy gradient norm in time for various mesh spacings (labeled), and the fourth row shows the convergence of Δz in time.

Table 2
Comparison of the equilibrium sheet deflection Δz as the mesh spacing d is decreased for the triangular lattice model (denoted TL) and the finite difference model (denoted FD) with two values of one of the Poisson ratio terms (denoted ν_B).

d_{TL}	Δz_{TL}	d_{FD}	Δz_{FD}, $\nu_B = -1/3$	Δz_{FD}, $\nu_B = 1/3$
1/16	0.70710	1/16	0.69991	0.71035
1/24	0.72011	1/24	0.69884	0.70986
1/48	0.71124	1/32	0.69851	0.70966
1/80	0.71165	1/40	0.69837	0.70950
1/112	0.71178	1/48	0.69829	0.70948

We have illustrated the behavior of the algorithms in three simple cases. We've seen close agreement in two equilibria found with a steady reference metric, and somewhat less agreement in a dynamical problem with a unidirectional traveling wave metric. We now proceed to illustrate some other basic features of the buckling behavior and dynamics, with the triangular lattice approach only for brevity.

If a static reference metric cannot be realized by a surface in $\mathbb{R}^3$, the sheet has nonzero stretching energy, and in general becomes unstable to out-of-plane buckling for sufficiently small h [66]. Intuitively, buckling allows a reduction in stretching energy at the expense of bending energy. The relative cost of bending decreases with decreasing h, making buckling more favorable. For the static metric with $\eta = \eta_1$ in (34), in Fig. 6 we plot a computational estimate of the

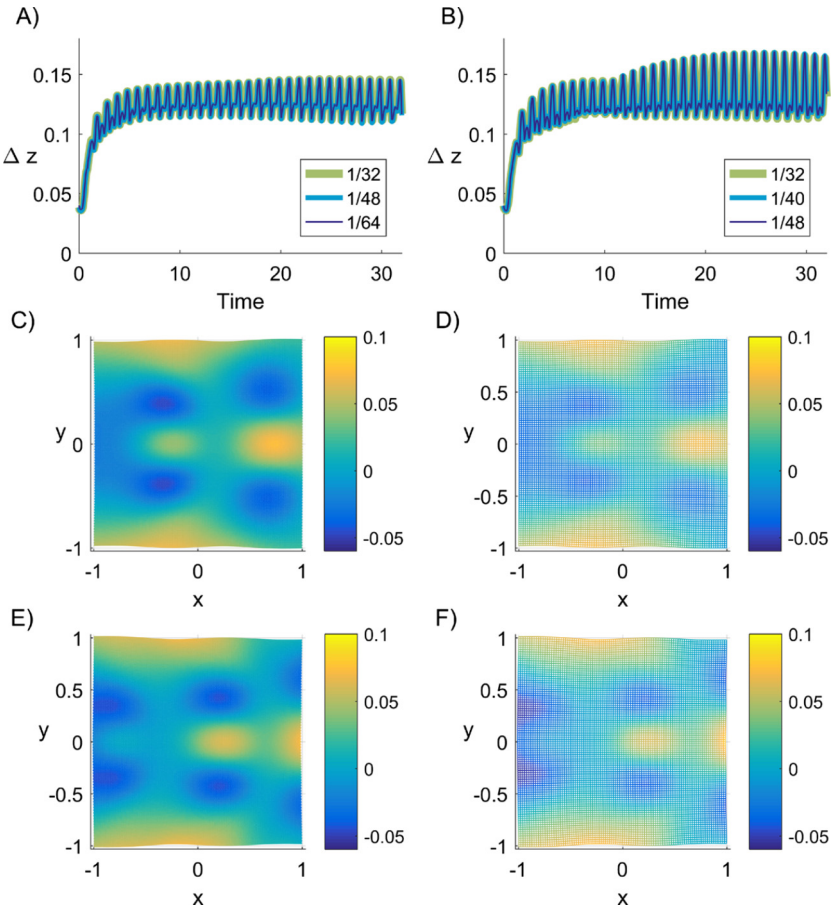

Fig. 5. A comparison of sheet dynamics with the triangular lattice and finite difference algorithms with reference metric factor $\eta = \eta_2$ in (35), a unidirectional traveling wave, starting from a nearly flat sheet. The physical parameters are $A = 0.03$, $k = 1$, $h = 0.03$, $\mu = 1000$, and $\nu = 1/3$. (A) The z-deflection over time for the triangular lattice algorithm for lattice spacings $d_{TL} = 1/32$, 1/48, and 1/64. (B) The z-deflection over time for the finite difference algorithm for grid spacings $d_{FD} = 1/32$, 1/40, and 1/48. Distributions of z deflection at times $t = 31.5$ and 32 are shown in panels (C) and (E) for the triangular lattice and (D) and (F) for the finite difference method, respectively.

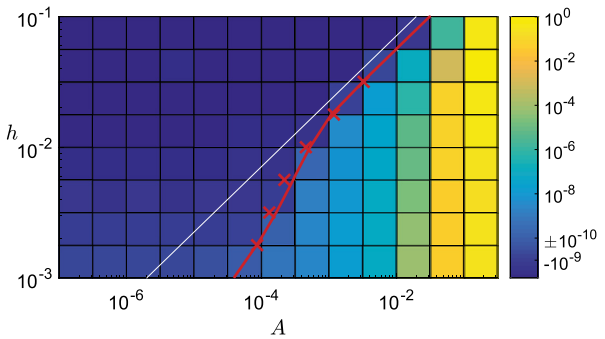

Fig. 6. Change in out-of-plane deflection from $t = 0$ to $t = 2$ for a unit hexagon with a small initial deflection $z = 10^{-8} x_1 x_2$, and imposed reference metric (34) with $k = 1$, varying metric factor amplitude A (horizontal axis) and varying sheet thickness h (vertical axis). The damping constant $\mu = 12.6$ and the mesh spacing $d = 1/33$. The solid red line shows the locus of zero change in deflection, essentially the "buckling threshold." The red crosses show, at several values of h, the values of A on the buckling threshold with a finer mesh spacing, 1/66. The white line shows the scaling $A \sim h^2$.

"buckling threshold"—for various $A \in [10^{-5}, 10^{-1}]$, the values of h at which buckling occurs. Here buckling is defined by whether a small initial deflection ($z = 10^{-8} x_1 x_2$) grows after two time units, with a certain damping constant ($\mu = 12.6$). Changes in the time interval and damping constant have only a slight effect on the buckling threshold, plotted as a red solid line for $d = 1/33$. The mesh spacing becomes more important at smaller h, where buckling deformations may occur with a smaller wavelength due to the decreased bending energy. To check the effect of mesh refinement, we repeat the

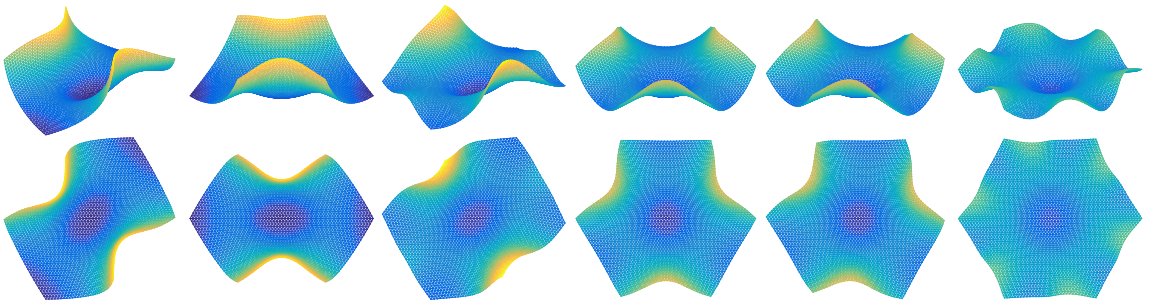

Fig. 7. A selection of six buckled equilibria of the unit hexagon. Each is shown in two views: the top row gives views from 60 degrees with respect to the z-axis, and the bottom row gives views along the z-axis. The sheet thickness is $h = 0.03$ and the imposed reference metric factor is $\eta = \eta_1$ given in (34) with $A = 0.1$ and $k = 1$. The equilibria are obtained by starting from different initial perturbations, with lattice spacing $d = 1/33$.

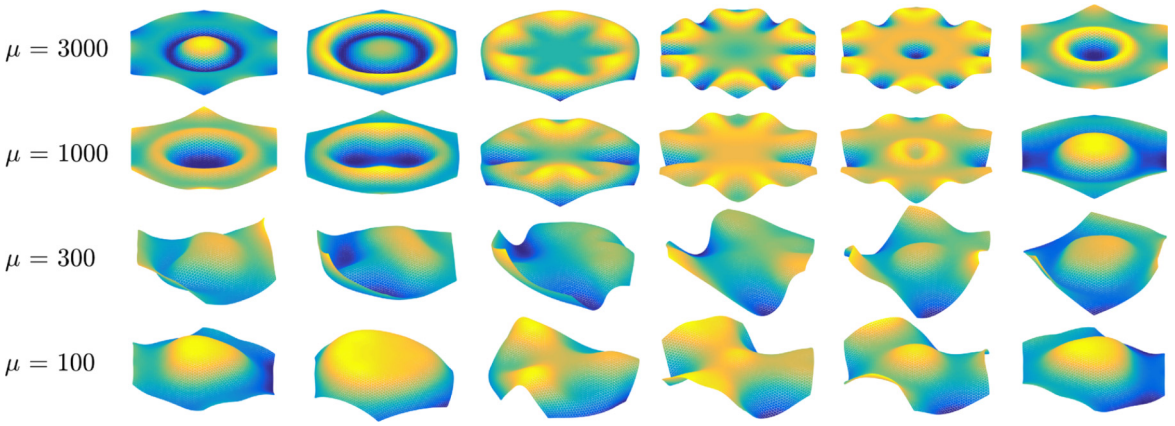

Fig. 8. Snapshots of a unit hexagon, from $t = 19$ to 20 in time increments of 0.2 (from left to right) with different damping constants μ (top to bottom), metric factor amplitude $A = 0.1$ in (36) and $h = 0.03$. The colors show the z coordinate value, and the color scale is scaled to the minimum and maximum z coordinate value of each sheet.

computations with $d = 1/66$ at selected points and obtain the red crosses. The white line shows the scaling $A \sim h^2$, which approximately matches the buckling threshold data presented in [66] for a different reference metric. Our data appear to follow this trend for $h \geq 0.01$. Deviations at smaller h are likely due to the finite mesh spacing.

Next, we study the postbuckling behavior, again with the static metric factor $\eta = \eta_1$ in (34) but with $A = 0.1$, $k = 1$, and different initial perturbations of the form $z = cr^m \sin(m\phi)$, where r is the initial distance of sheet points from the hexagon center, ϕ is the azimuthal angle (with respect to the hexagon center), and m is the azimuthal wavenumber, an integer from 2 to 6. The amplitude c ranges from 0 to 0.1, and μ ranges from 1 to 1000. We obtain buckling into various equilibria akin to those studied by [66] with other radially symmetric reference metrics. We show six equilibria in Fig. 7, in two views (top and bottom rows). The first three (starting at the left) have a twofold azimuthal rotational symmetry, but are distinct configurations. The second has an additional bilateral symmetry and the third has an additional pair of (small) local maxima along the sheet edges. The fourth and fifth have a threefold rotational symmetry, and the fourth has bilateral symmetries in addition. The sixth has a sixfold rotational symmetry. These are only a selection of local equilibria for a given static reference metric, and illustrate the complexity of the energy landscape for such sheets, even without dynamics and/or a time-dependent reference metric.

6.1. Parameter sweeps

We next study the effects of parameters on the sheet dynamics, using the reference metric factor $\eta = \eta_3$ in (36), a radial traveling wave. We perform a sequence of parameter sweeps, varying one of A, h, or μ while keeping the others fixed. We fix the wavenumber k at 1 in all cases. If k is much smaller, the sheet does not buckle because the reference metric is almost uniform, and planar dilation/contraction is preferred energetically. If k is much larger, buckling is also inhibited because the reference metric averaged over a local region approaches the identity tensor. As a base case, we take $A = 0.1$, $\mu = 1000$, and $h = 0.03$, and vary each physical parameter in turn with numerical parameters $d = 1/33$ and $\Delta t = 0.005$ (sufficiently small that further decreases do not qualitatively change the results). We initialize the sheet with a small out-of-plane deflection ($z = 0.02(x_1^4 + x_2^4)$, $-1 \leq x_1 = x, x_2 = y \leq 1$).

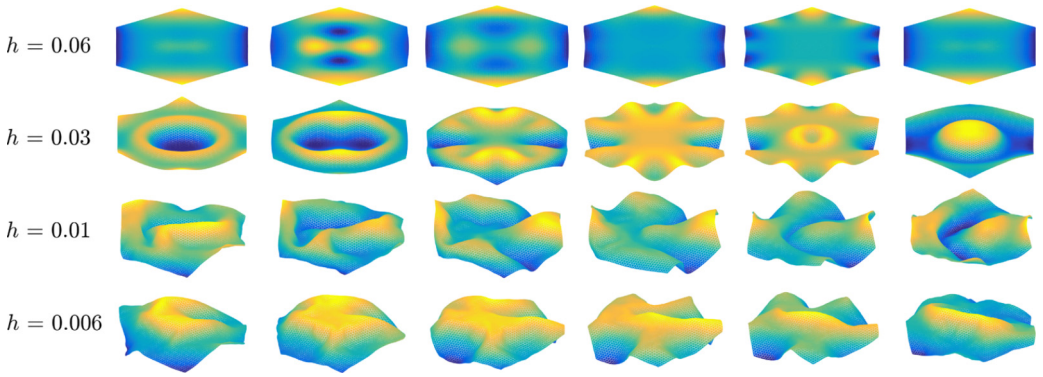

Fig. 9. Snapshots of sheet dynamics with various sheet thicknesses h (top to bottom), from $t = 19$ to 20 in time increments of 0.2 (from left to right). Here $A = 0.1$ and $\mu = 1000$.

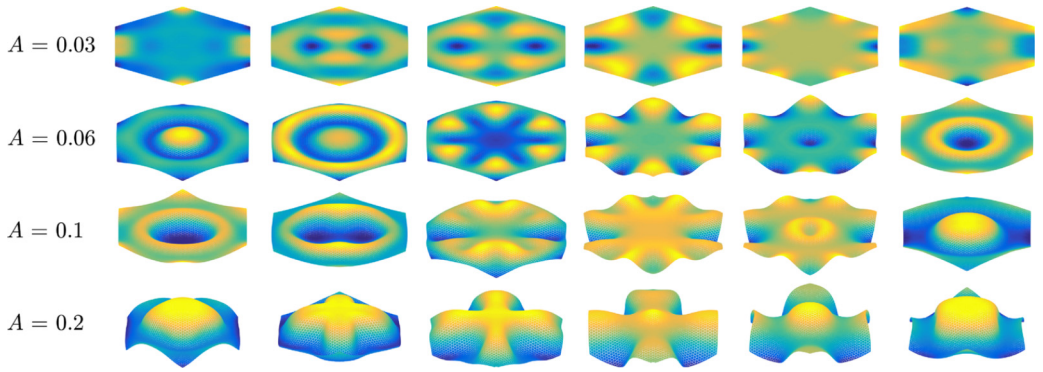

Fig. 10. Snapshots of sheet dynamics with various metric factor amplitudes A (in (36)), from $t = 19$ to 20 in time increments of 0.2 (from left to right). Here $h = 0.03$ and $\mu = 1000$.

In Fig. 8 we show snapshots of a unit hexagon from $t = 19$ to 20 in time increments of 0.2 (from left to right), for four different values of μ, with $A = 0.1$ and $h = 0.03$. When μ is large, the sheet responds more slowly to the reference metric. The tendency is to oscillate about a mean state of no deformation (because the long-time-average reference metric is the identity tensor), and at sufficiently large μ the sheet does not buckle out of plane. At the largest μ (3000), the dynamics are essentially periodic (with period 2, so only a half-period is shown; the position at time $t+1$ is that at time t but reflected in the $z = 0$ plane). The out-of-plane deflection is smaller and more symmetric than at smaller μ, where the dynamics become more chaotic and asymmetric. At smaller μ, the sheet moves more rapidly through the complicated, time-dependent elastic energy landscape. At $\mu = 1000$, the sheet deflection $\Delta z(t)$ has a large component with the same period as the reference metric, but also large components that are not periodic. At $\mu = 300$, bilateral symmetry is lost, while at $\mu = 100$, the sheet almost assumes a threefold symmetry.

Next, we vary h, with $A = 0.1$ and $\mu = 1000$. Snapshots are shown in Fig. 9. With larger h, bending is relatively more costly, so the deformation is smoother, and at sufficiently large h the sheet relaxes back to a planar state ($h = 0.06$). At smaller h, the sheet motion is more chaotic and asymmetric, as for decreasing μ. Notably, at smaller h fine wrinkling features appear, and the deformation is far from any kind of symmetry. Eventually the sheet may intersect itself (not shown) because forces due to self-contact are not included.

We vary A next, with $h = 0.03$ and $\mu = 1000$. Here (Fig. 10) there is a sequence of dynamics from slow relaxation to planar motions ($A = 0.03$), to periodic and symmetric ($A = 0.06$, with period 2), to aperiodic but still bilaterally symmetric ($A = 0.1$ and 0.2). At larger A the deflection amplitude increases but the deformation remains relatively smooth, and in this sense the dynamics are more similar to smaller μ than to smaller h.

Finally, we consider the effect of the sheet shape on the dynamics. We consider the two cases with periodic dynamics above, ($A = 0.1$, $\mu = 3000$) in Fig. 8 and ($A = 0.06$, $\mu = 1000$) in Fig. 10, both with $h = 0.03$. In the top two rows of Fig. 11, we compare the hexagonal sheet snapshots with those of a square sheet with the same parameters. Both sheets have width 2 when the reference metric is the identity. The bottom two rows make the same comparison with $A = 0.06$ and $\mu = 1000$. At each time, the hexagonal and square sheets have qualitative similarities. At the first time (leftmost snapshots), the sheets have a central peak. At the second time, an upward ring (yellow) appears. Third, the ring breaks up into an array of peaks with sixfold symmetry for the hexagons, and either six- or fourfold symmetry for the squares. Fourth, the peaks reach the sheet boundary. Fifth, a central trough forms, and sixth, it widens and is surrounded by an upward ring. The main differences between the squares and hexagons are that the squares more often have a fourfold rather than sixfold

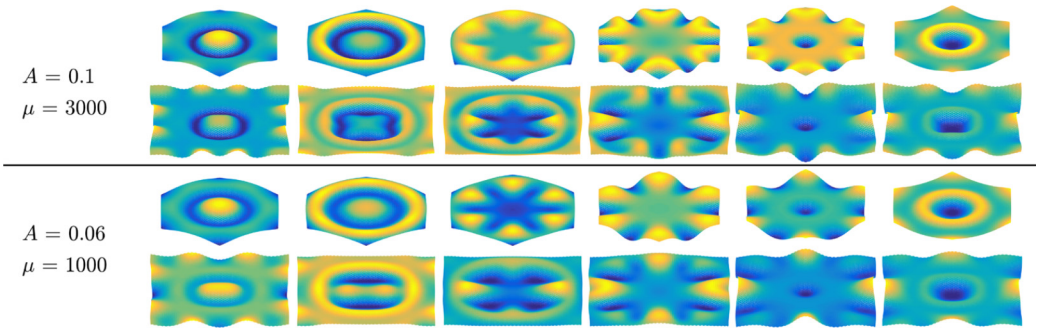

Fig. 11. Comparisons of the dynamics of hexagonal and square sheets with $A = 0.1$ and $\mu = 3000$ in the top two rows and $A = 0.06$ and $\mu = 1000$ in the bottom two rows. All other parameters and initial conditions are the same as in Figs. 8 and 10 (e.g. $h = 0.03$), and the snapshots run from $t = 19$ to 20 in time increments of 0.2 (from left to right).

symmetry, the maximum deflections of the squares are larger, and the squares have a significant nonperiodic component in the dynamics. The comparison illustrates that periodic dynamics can be somewhat sensitive to sheet shape, which is perhaps not surprising given that chaotic dynamics are common and small changes in the parameters can shift periodic dynamics to chaotic dynamics. In Appendix B we extend the comparison to ranges of values of μ and A, including cases that are nonperiodic (but still with approximate bilateral symmetry). We find that the sheet shape strongly affects the preferred azimuthal mode of deformation across these ranges of parameter values.

7. Conclusion

We have presented semi-implicit algorithms that can simulate the dynamics of thin elastic sheets with large time steps. We focus on the case of elastic sheets with nontrivial steady or time-varying reference metrics in overdamped dynamics, but the methods should apply to other problems with internal or external forcing. The first algorithm simulates a triangular lattice mesh, and uses a splitting of the stretching force that has been used previously for computer graphics simulations of hair and cloth [40,43]. The semi-implicit bending force uses a biharmonic operator with free-edge boundary conditions. The algorithm was found to be unconditionally numerically stable for a time-periodic reference metric. The second algorithm simulates a rectangular grid with finite-difference derivatives of the energy, and allows for general values of the Poisson ratio (and unlike the triangular lattice, a consistent value in all terms of the bending and stretching energies). The semi-implicit finite difference algorithm is analogous to that for the triangular lattice, involving a stretching force operator with zero equilibrium metric, and the biharmonic operator for an approximate bending force. The finite difference algorithm is not unconditionally stable, but typically has a maximum stable time step two to three orders of magnitude greater than that of an explicit scheme.

The two algorithms agree very closely for the deformation of a square sheet under a static reference metric, even allowing a different Poisson ratio ($-1/3$ instead of $1/3$) in one of the bending energy terms. There is more disagreement in the deflection amplitude and pattern for a unidirectional traveling wave reference metric, but the dynamics are qualitatively similar. For the triangular lattice, we see phenomena similar to those reported previously with different radially-symmetric reference metrics [66]: a 1/2-power-law scaling of the buckling threshold in the space of sheet thickness and reference metric factor amplitude, and the presence of multiple stable equilibria with varying types of azimuthal and bilateral symmetries. For the case of a radial traveling wave reference metric, we showed some of the basic effects of sheet and metric parameters. In general, as the metric factor amplitude increases, the sheet thickness decreases, or the damping parameter decreases, the sheet moves from flat, periodic oscillations, to buckled periodic oscillations with various types of symmetries, and then to buckled motions with a combination of periodic and nonperiodic components, and varying degrees of symmetry/asymmetry. Below a critical sheet thickness, the motions have little semblance of symmetry or periodicity.

Declaration of competing interest

The authors declare that they have no known competing financial interests or personal relationships that could have appeared to influence the work reported in this paper.

Acknowledgements

We acknowledge support from the Michigan Institute for Computational Discovery and Engineering (MICDE).

Appendix A. Bending force

We denote the discrete biharmonic operator on the triangular mesh with free-edge boundary conditions as $\tilde{\Delta}^2_{x_1,x_2}$, and because it is independent of the sheet configuration we may derive it for a sheet that is a portion of a flat triangular lattice

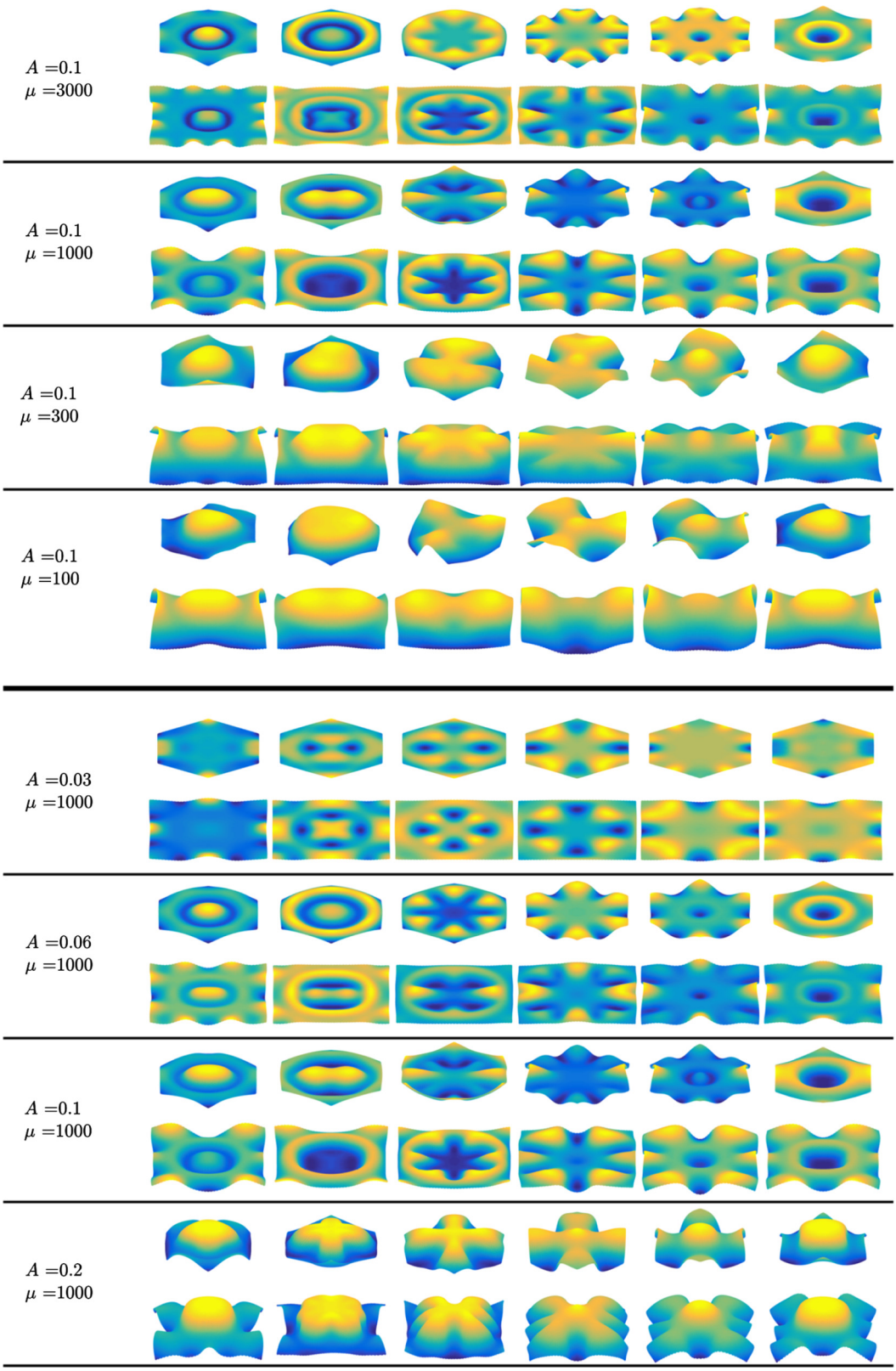

Fig. 12. Comparisons of the dynamics of hexagonal and square sheets with various μ at $A = 0.1$ (top eight rows) and various A at $\mu = 1000$ (bottom eight rows). All other parameters and initial conditions are the same as in Figs. 8 and 10 (e.g. $h = 0.03$), and the snapshots run from $t = 19$ to 20 in time increments of 0.2 (from left to right).

with edge length d. $\tilde{\Delta}^2_{x_1,x_2}$ is a mapping from (small) out-of-plane displacements at each point to the bending force at that point. The mapping is a sum of the force-displacement mappings for each pair of adjacent equilateral triangles, because the bending energy is also a sum over such units. For the four vertices in a given pair of neighboring triangles, a unit upward displacement of one of the two outer vertices (those not on the shared edge) yields a downward bending force at each of the outer vertices, equal by symmetry, and an upward force at each of the inner two vertices (those on the shared edge), equal and opposite to those at the outer vertices, to give net force and torque balance. The forces are proportional to the displacement by a constant that gives the desired bending modulus of the sheet. The bottom row of Fig. 2 shows examples of the stencils for this biharmonic operator at a few mesh points: an interior point (analogous to the 13-point biharmonic stencil on a rectangular mesh), a next-to-boundary point, and a boundary point. The discrete biharmonic operator $\tilde{\Delta}^2_{x_1,x_2}$ has these stencil values multiplied by the triangle altitudes raised to the -4 power $(\sqrt{3}d/2)^{-4}$, while the linearized bending force operator has instead the same stencil values multiplied by $(\sqrt{3}d/2)^{-2}$ because the bending force is the gradient of the bending energy, which is approximately the biharmonic of the deflection multiplied by the sheet area per vertex.

Appendix B. Effect of sheet shape on dynamics

In Fig. 12 we present additional comparisons of hexagonal and square sheets' dynamics, now for a range of μ at fixed $A = 0.1$ (top half of figure), and for a range of A at fixed $\mu = 1000$ (bottom half of figure). In each pair of rows, the hexagonal sheet is at the top and the square sheet is at the bottom. For each pair, the qualitative features of the deformations (such as the typical wavelengths of the out-of-plane deflection) are similar, but the numbers of local maxima and minima—i.e. the buckled modes—differ in several cases.

References

[1] C.R. Calladine, Theory of Shell Structures, Cambridge University Press, 1983.
[2] L.B. Freund, S. Suresh, Thin Film Materials: Stress, Defect Formation and Surface Evolution, Cambridge University Press, Cambridge, 2004.
[3] Shahaf Armon, Efi Efrati, Raz Kupferman, Eran Sharon, Geometry and mechanics in the opening of chiral seed pods, Science 333 (6050) (2011) 1726–1730.
[4] B. Audoly, A. Boudaoud, Self-similar structures near boundaries in strained systems, Phys. Rev. Lett. 91 (8) (2003).
[5] C.D. Santangelo, Buckling thin disks and ribbons with non-Euclidean metrics, Europhys. Lett. 86 (3) (2009).
[6] John A. Gemmer, Shankar C. Venkataramani, Shape selection in non-Euclidean plates, Physica D 240 (19) (2011) 1536–1552.
[7] Eran Sharon, Swell approaches for changing polymer shapes, Science 335 (6073) (2012) 1179–1180.
[8] Eran Sharon, Hillel Aharoni, Frustrated shapes, Nat. Mater. 15 (7) (2016) 707–709.
[9] E. Efrati, E. Sharon, R. Kupferman, Elastic theory of unconstrained non-Euclidean plates, J. Mech. Phys. Solids 57 (4) (2009) 762–775.
[10] Efi Efrati, Eran Sharon, Raz Kupferman, The metric description of elasticity in residually stressed soft materials, Soft Matter 9 (34) (2013) 8187–8197.
[11] Jun-Hee Na, Arthur A. Evans, Jinhye Bae, Maria C. Chiappelli, Christian D. Santangelo, Robert J. Lang, Thomas C. Hull, Ryan C. Hayward, Programming reversibly self-folding origami with micropatterned photo-crosslinkable polymer trilayers, Adv. Mater. 27 (1) (2015) 79–85.
[12] Yael Klein, Efi Efrati, Eran Sharon, Shaping of elastic sheets by prescription of non-Euclidean metrics, Science 315 (5815) (2007) 1116–1120.
[13] Jungwook Kim, James A. Hanna, Myunghwan Byun, Christian D. Santangelo, Ryan C. Hayward, Designing responsive buckled surfaces by halftone gel lithography, Science 335 (6073) (2012) 1201–1205.
[14] Zi Liang Wu, Michael Moshe, Jesse Greener, Heloise Therien-Aubin, Zhihong Nie, Eran Sharon, Eugenia Kumacheva, Three-dimensional shape transformations of hydrogel sheets induced by small-scale modulation of internal stresses, Nat. Commun. 4 (2013) 1586.
[15] T.H. Ware, M.E. McConney, J.J. Wie, V.P. Tondiglia, T.J. White, Voxelated liquid crystal elastomers, Science 347 (6225) (2015) 982–984.
[16] Timothy J. White, Dirk J. Broer, Programmable and adaptive mechanics with liquid crystal polymer networks and elastomers, Nat. Mater. 14 (11) (2015) 1087–1098.
[17] A. Sydney Gladman, Elisabetta A. Matsumoto, Ralph G. Nuzzo, L. Mahadevan, Jennifer A. Lewis, Biomimetic 4D printing, Nat. Mater. 15 (4) (2016) 413.
[18] Yen-Chih Lin, Ji-Ming Sun, Jen-Hao Hsiao, Yeukuang Hwu, C.L. Wang, Tzay-Ming Hong, Spontaneous emergence of ordered phases in crumpled sheets, Phys. Rev. Lett. 103 (2009) 263902.
[19] B. Roman, J. Bico, Elasto-capillarity: deforming an elastic structure with a liquid droplet, J. Phys. Condens. Matter 22 (49) (2010) 493101.
[20] Hillel Aharoni, Eran Sharon, Direct observation of the temporal and spatial dynamics during crumpling, Nat. Mater. 9 (12) (2010) 993–997.
[21] Joseph D. Paulsen, Vincent Demery, K. Bugra Toga, Zhanlong Qiu, Thomas P. Russell, Benny Davidovitch, Narayanan Menon, Geometry-driven folding of a floating annular sheet, Phys. Rev. Lett. 118 (4) (2017) 27.
[22] R. Yoshida, T. Takahashi, T. Yamaguchi, H. Ichijo, Self-oscillating gel, J. Am. Chem. Soc. 118 (21) (1996) 5134–5135.
[23] Shingo Maeda, Yusuke Hara, Takamasa Sakai, Ryo Yoshida, Shuji Hashimoto, Self-walking gel, Adv. Mater. 19 (21) (2007) 3480.
[24] O. Tabata, H. Hirasawa, S. Aoki, R. Yoshida, E. Kokufuta, Ciliary motion actuator using self-oscillating gel, Sens. Actuators A, Phys. 95 (2–3) (2002) 234–238.
[25] O. Tabata, H. Kojima, T. Kasatani, Y. Isono, R. Yoshida, Chemo-mechanical actuator using self-oscillating gel for artificial cilia, in: MEMS-03: IEEE the Sixteenth Annual International Conference on Micro Electro Mechanical Systems, Proceedings: IEEE Micro Electro Mechanical Systems, IEEE, 2003, pp. 12–15.
[26] Shingo Maeda, Yusuke Hara, Ryo Yoshida, Shuji Hashimoto, Peristaltic motion of polymer gels, Angew. Chem., Int. Ed. Engl. 47 (35) (2008) 6690–6693.
[27] Yusuke Shiraki, Ryo Yoshida, Autonomous intestine-like motion of tubular self-oscillating gel, Angew. Chem., Int. Ed. Engl. 51 (25) (2012) 6112–6116.
[28] V.V. Yashin, A.C. Balazs, Modeling polymer gels exhibiting self-oscillations due to the Belousov-Zhabotinsky reaction, Macromolecules 39 (6) (2006) 2024–2026.
[29] Olga Kuksenok, Victor V. Yashin, Anna C. Balazs, Mechanically induced chemical oscillations and motion in responsive gels, Soft Matter 3 (9) (2007) 1138–1144.
[30] Victor V. Yashin, Anna C. Balazs, Theoretical and computational modeling of self-oscillating polymer gels, J. Chem. Phys. 126 (12) (2007) 124707.
[31] Olga Kuksenok, Debabrata Deb, Pratyush Dayal, Anna C. Balazs, Modeling chemoresponsive polymer gels, Annu. Rev. Chem. Biomol. Eng. 5 (1) (2014) 35–54, PMID: 24498954424498954.
[32] Mila Boncheva, Stefan A. Andreev, L. Mahadevan, Adam Winkleman, David R. Reichman, Mara G. Prentiss, Sue Whitesides, George M. Whitesides, Magnetic self-assembly of three-dimensional surfaces from planar sheets, Proc. Natl. Acad. Sci. USA 102 (11) (2005) 3924–3929.

[33] Silas Alben, Michael P. Brenner, Self-assembly of flat sheets into closed surfaces, Phys. Rev. E 75 (5) (2007) 056113.
[34] Silas Alben, Bavani Balakrisnan, Elisabeth Smela, Edge effects determine the direction of bilayer bending, Nano Lett. 11 (6) (2011) 2280–2285.
[35] Silas Alben, Bending of bilayers with general initial shapes, Adv. Comput. Math. 41 (1) (2015) 1–22.
[36] Shravan K. Veerapaneni, Abtin Rahimian, George Biros, Denis Zorin, A fast algorithm for simulating vesicle flows in three dimensions, J. Comput. Phys. 230 (14) (2011) 5610–5634.
[37] H.H. Rosenbrock, Some general implicit processes for the numerical solution of differential equations, Comput. J. 5 (4) (1963) 329–330.
[38] David Gottlieb, Steven A. Orszag, Numerical Analysis of Spectral Methods: Theory and Applications, vol. 26, SIAM, 1977.
[39] Thomas Y. Hou, John S. Lowengrub, Michael J. Shelley, Removing the stiffness from interfacial flows with surface tension, J. Comput. Phys. 114 (2) (1994) 312–338.
[40] Mathieu Desbrun, Peter Schröder, Alan Barr, Interactive animation of structured deformable objects, in: Graphics Interface, vol. 99, 1999, p. 10.
[41] Bernhard Eberhardt, Olaf Etzmuß, Michael Hauth, Implicit-explicit schemes for fast animation with particle systems, in: Computer Animation and Simulation 2000, Springer, 2000, pp. 137–151.
[42] Thomas Y. Hou, John S. Lowengrub, Michael J. Shelley, Boundary integral methods for multicomponent fluids and multiphase materials, J. Comput. Phys. 169 (2) (2001) 302–362.
[43] Andrew Selle, Michael Lentine, Ronald Fedkiw, A mass spring model for hair simulation, ACM Trans. Graph. 27 (2008) 64.
[44] Silas Alben, An implicit method for coupled flow–body dynamics, J. Comput. Phys. 227 (10) (2008) 4912–4933.
[45] Silas Alben, Simulating the dynamics of flexible bodies and vortex sheets, J. Comput. Phys. 228 (7) (2009) 2587–2603.
[46] Hsiao-Yu Chen, Arnav Sastry, Wim M. van Rees, Etienne Vouga, Physical simulation of environmentally induced thin shell deformation, ACM Trans. Graph. 37 (4) (2018) 146.
[47] H.S. Seung, D.R. Nelson, Defects in flexible membranes with crystalline order, Phys. Rev. A 38 (2) (1988) 1005–1018.
[48] Warner Tjardus Koiter, On the nonlinear theory of thin elastic shells, Proc. K. Ned. Akad. Wet., Ser. B 69 (1966) 1–54.
[49] Philippe G. Ciarlet, Un modèle bi-dimensionnel non linéaire de coque analogue à celui de wt Koiter, C. R. Acad. Sci., Sér. 1 Math. 331 (5) (2000) 405–410.
[50] Roman Vetter, Norbert Stoop, Thomas Jenni, Falk K. Wittel, Hans J. Herrmann, Subdivision shell elements with anisotropic growth, Int. J. Numer. Methods Eng. 95 (9) (2013) 791–810.
[51] Efi Efrati, Yael Klein, Hillel Aharoni, Eran Sharon, Spontaneous buckling of elastic sheets with a prescribed non-Euclidean metric, Physica D 235 (1–2) (2007) 29–32.
[52] Jorge Nocedal, Stephen Wright, Numerical Optimization, Springer Science & Business Media, 2006.
[53] Ernst Hairer, Syvert P. Norsett, Gerhard Wanner, Solving Ordinary Differential Equations II: Stiff Problems, Springer, 1987.
[54] Gerhard Gompper, Daniel M. Kroll, Fluctuations of polymerized, fluid and hexatic membranes: continuum models and simulations, Curr. Opin. Colloid Interface Sci. 2 (4) (1997) 373–381.
[55] Alexander E. Lobkovsky, T.A. Witten, Properties of ridges in elastic membranes, Phys. Rev. E 55 (2) (1997) 1577.
[56] Jack Lidmar, Leonid Mirny, David R. Nelson, Virus shapes and buckling transitions in spherical shells, Phys. Rev. E 68 (5) (2003) 051910.
[57] G.A. Vliegenthart, G. Gompper, Forced crumpling of self-avoiding elastic sheets, Nat. Mater. 5 (3) (2006) 216.
[58] Eleni Katifori, Silas Alben, Enrique Cerda, David R. Nelson, Jacques Dumais, Foldable structures and the natural design of pollen grains, Proc. Natl. Acad. Sci. USA 107 (17) (2010) 7635–7639.
[59] Etienne Couturier, J. Dumais, E. Cerda, Elenei Katifori, Folding of an opened spherical shell, Soft Matter 9 (34) (2013) 8359–8367.
[60] Chloe M. Funkhouser, Rastko Sknepnek, Monica Olvera, De La Cruz, Topological defects in the buckling of elastic membranes, Soft Matter 9 (1) (2013) 60–68.
[61] Duanduan Wan, David R. Nelson, Mark J. Bowick, Thermal stiffening of clamped elastic ribbons, Phys. Rev. B 96 (1) (2017) 014106.
[62] David R. Nelson, Tsvi Piran, Steven Weinberg, Statistical Mechanics of Membranes and Surfaces, World Scientific, 2004.
[63] Bernd Schmidt, Fernando Fraternali, Universal formulae for the limiting elastic energy of membrane networks, J. Mech. Phys. Solids 60 (1) (2012) 172–180.
[64] Brian Anthony DiDonna, Scaling of the buckling transition of ridges in thin sheets, Phys. Rev. E 66 (1) (2002) 016601.
[65] Joel L. Weiner, On a problem of Chen, Willmore et al., Indiana Univ. Math. J. 27 (1) (1978) 19–35.
[66] Efi Efrati, Eran Sharon, Raz Kupferman, Buckling transition and boundary layer in non-Euclidean plates, Phys. Rev. E 80 (1) (2009).